Research article **Open Access**

Massimo Rippa*, Riccardo Castagna, Marianna Pannico, Pellegrino Musto, Volodymyr Tkachenko, Jun Zhou and Lucia Petti

Engineered plasmonic Thue-Morse nanostructures for LSPR detection of the pesticide Thiram

DOI 10.1515/nanoph-2016-0146
Received August 14, 2016; revised November 21, 2016; accepted December 7, 2016

Abstract: In this paper, the size- and shape-dependent spectral characteristics of plasmonic nanostructures based on the Thue-Morse (ThMo) sequence are investigated in theory and experiment. We designed, fabricated, and characterized nine different Au nanopillars (NPs) lattices to evaluate their use as nanosensors based on localized surface plasmon resonances (LSPR). The extinction spectra and the bulk refractive index sensitivity (m) are compared to three selected shapes of the NPs (square, circular, and triangular) with different minimum interparticle distance. The maximum m of 275 nm/RIU is obtained for a ThMo pattern with square NPs. Finally, a detection limit of 260 pM (62 pg/ml) of Thiram pesticide has been achieved using an LSPR nanosensor based on an optimized ThMo pattern with triangular NPs employing a phase-sensitive setup to increase the figure-of-merit (FOM) of the sensor.

Keywords: plasmonic; nanostructures; sensors; LSPR; Thiram.

***Corresponding author: Massimo Rippa,** Institute of Applied Sciences and Intelligent Systems "E. Caianiello" of CNR, Via Campi Flegrei 34, 80078 Pozzuoli, Italy, e-mail: m.rippa@isasi.cnr.it
Riccardo Castagna, Marianna Pannico and Lucia Petti: Institute of Applied Sciences and Intelligent Systems "E. Caianiello" of CNR, Via Campi Flegrei 34, 80078 Pozzuoli, Italy
Pellegrino Musto: Institute for Polymers, Composites and Biomaterials of CNR, 80078 Pozzuoli, Italy
Volodymyr Tkachenko: Institute of Applied Sciences and Intelligent Systems "E. Caianiello" of CNR, Via Campi Flegrei 34, 80078 Pozzuoli, Italy; and Physics Department, University of Naples "Federico II", 80126 Naples, Italy
Jun Zhou: Institute of Applied Sciences and Intelligent Systems "E. Caianiello" of CNR, Via Campi Flegrei 34, 80078 Pozzuoli, Italy; and Institute of Photonics, Faculty of Science, Ningbo University, Ningbo 315211, China

1 Introduction

In the last decade, the development of nanosensors based on extraordinary plasmonic properties has attracted much attention for the detection and monitoring of environmental and biological agents [1–15]. Among the variety of devices available, localized surface plasmon resonance (LSPR)-based nanosensors are considered one of the most powerful tools for analyte investigation [16, 17]. They work by transducing small refractive index variations near the metallic surface of the nanoelements into a measurable wavelength shift response. LSPR nanosensors have the notable advantages of a label-free detection and can be engineered to provide devices with very low limit of detection (LOD) for specific molecules. Furthermore, compared with other plasmonic sensors based on surface plasmonic resonance (SPR) or surface enhanced Raman spectroscopy (SERS), LSPR nanosensors allow to realize low-cost prototype and portable systems, do not require a temperature control, and can be implemented by the use of an easy instrumental setup. Thanks to these advantages, LSPR sensing system has been applied in a wide range of fields, such as food safety, environmental monitoring, and medical diagnostics [18–25].

Plasmonic properties and near-field distribution affect the main characteristics of these nanosensors such as sensitivity, LOD, and reproducibility. However, as widely discussed and studied in literature, both plasmonic properties and near-field distribution can be controlled and tuned conveniently by the change of the shape, size, and geometry of the nanopattern [26–37]. In this regard, it has been shown that nanostructures based on aperiodic geometries can allow an exceptional degree of control on the light properties to provide strongly enhanced near fields and to enable very sensitive plasmonic devices [38–44]. As reported in literature [44, 45], aperiodic patterns provide the necessary balance between their resonant modes and the spatial distribution of large field intensity over extended sensing areas, resulting in largely improved sensitivity respect to periodic grating sensors or photonic

crystals cavities, which are limited by the small overlap of the analyte with the localized field.

In this work, we realized and compared engineered LSPR sensors based on a 2D Thue-Morse (ThMo) sequence with different geometries. Optical properties of the ThMo aperiodic pattern have been widely investigated, and their peculiarities (self-similar hierarchy of pseudoband-gap regions, omnidirectional reflectivity, and light emission enhancement) make such geometries an attractive candidate for the realization of high-performance multi-mode plasmonic nanosensors [45–50]. We fabricated them by the use of the electron beam lithography (EBL) process. EBL technique allows to realize highly reproducible nanopatterns by controlling with high precision size, shape and inter-particle distance, allowing the tuning of the plasmonic resonance in the visible and near-infrared range. The bulk refractive index sensitivity (m) of the devices has been evaluated, and a maximum value of 275 nm/RIU has been obtained for ThMo with square nanopillars (NPs).

The performance of the LSPR nanosensors for environmental analysis has been tested by the use of water solutions of a dithiocarbamate fungicide Thiram ($C_6H_{12}N_2S_4$). Thiram is a pesticide used on a variety of crops including fruit and vegetables, and it is toxic for human and, in particular, for most fish and aquatic organisms [51]. Phase-sensing approach is becoming an alternative to the traditional intensity sensing, thanks to the high sensitivity and signal-to-noise ratio that it allows [52]. In order to increase the figure-of-merit (FOM) of the sensor, we employed a phase-sensitive setup in the transmission based on common-path phase quadrature interferometry to evaluate the phase difference between the spectra measured along the axes of asymmetric NPs [52–54]. An LOD of 270 pM (62 pg/ml) was attained for Thiram using a ThMo pattern with triangular NPs, and our achievements have demonstrated how this new approach can dramatically boost FOM of refractive index sensing. We also performed SERS analysis to verify the physical adsorption of the Thiram molecules on the substrate as a function of different concentrations.

Although there have been many other attempts to detect Thiram using plasmonic sensors [55–60], to the best of our knowledge, this is the first time that this is done using the LSPR approach and nanosensors fabricated with a top-down technique. These results indicate that the LSPR nanosensors developed here are expected to demonstrate a wide range of applications for the detection of analytes of environmental and biological interest. Furthermore, our achievements open the way to use the ThMo pattern in dual-mode plasmonic sensors, combining LSPR and SERS analysis, making it more versatile for applications and more attractive from the cost-effectiveness ratio point of view.

2 Materials and methods

2.1 Nanostructures fabrication and morphological characterization

By using a Raith 150 EBL system, we fabricated nine 150 μm × 150 μm Au nanostructures based on ThMo arrays with circular, square, and triangular NPs and minimum interparticle distances a of 50, 80, and 100 nm. The side size d of NPs was, in all cases, 180 nm. Moreover, in order to make a comparison, we fabricated two 150 μm × 150 μm Au periodic crystals based on triangular NPs (nanoprisms) with sizes comparable to those used for ThMo patterns: triangles side $d = 180$ nm and minimum interparticle distance a of 50 and 100 nm.

In the fabrication process, a layer of 180-nm-thick styrene methyl acrylate-based polymer (ZEP from ZEONREX Electronic Chemicals) electron-sensitive resist was spin-coated on a 15-nm conductive ITO-coated glass substrate, baked at 170° for 5 min and exposed to 12.8-pA electron beam current. The patterns were generated in ZEP layer after development in a n-Amyl acetate solvent, then rinsed for 60 s in 1:3 MIBK:IPA solution (methyl isobutyl ketone:Isopropyl alcohol), followed by IPA rinse. All solvents were purchased from Sigma Aldrich. Au nanostructure arrays were created firstly by evaporating 2-nm Cr and 50-nm Au film (SISTEC CL-400C e-beam evaporator) to the ZEP surface and then with an additional lift-off step accomplished by immersing the substrate in N-methylpyrrolidinone (NMP) heated at 80°C for 5 min and then sprayed with a squizzle of NMP to remove the Au film. High-quality morphology nanostructures were characterized by both scanning electron microscopy (SEM – Raith 150) and atomic force microscopy (AFM-Ntegra Spectra, NT-MDT, Russia). The microscope images in Figure 1 refer to ThMo with $a = 50$ nm and show how both dimensions of the pillars and the step size of the nanostructures appear uniform and regular on the whole pattern.

2.2 FDTD simulations

In order to investigate both the near-field and the expected spectral response of the nano-arrays considered, we performed numerical calculations using the finite difference in time domain (FDTD, home-made

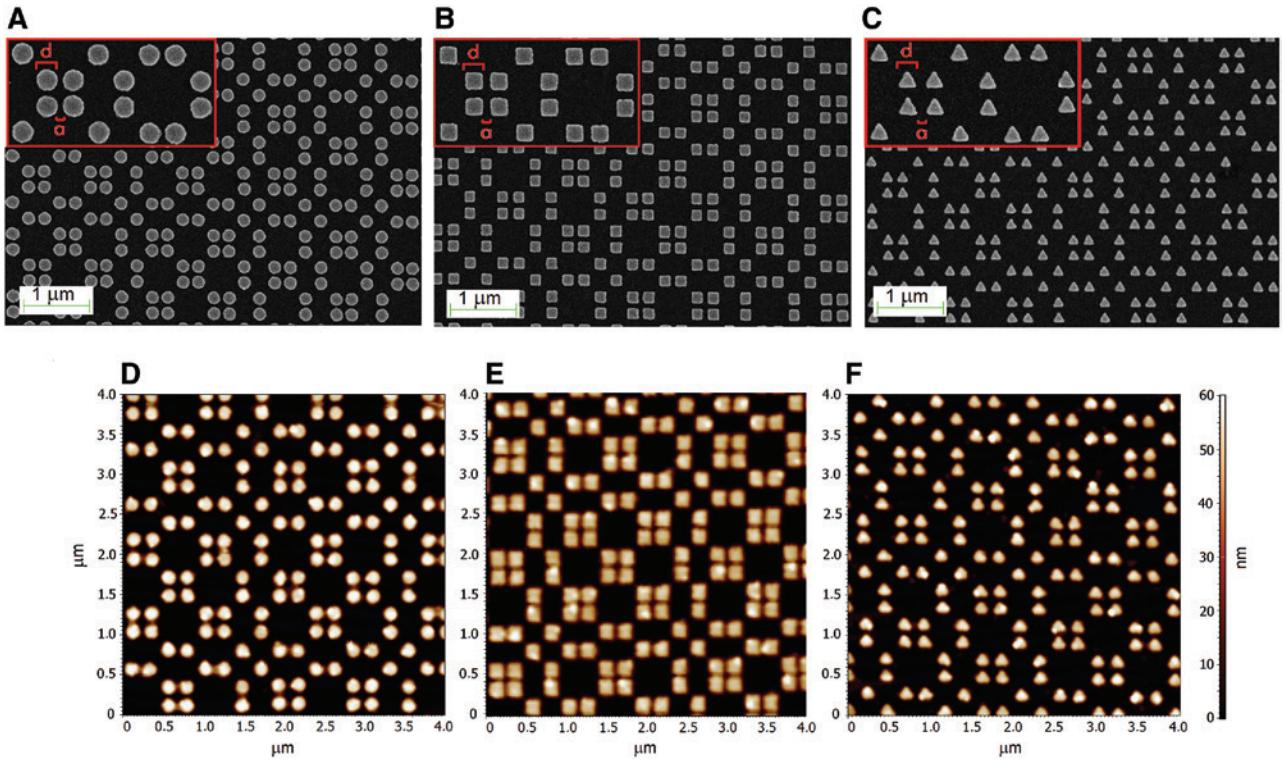

Figure 1: SEM images of ThMo nanopatterns with $d = 180$ nm, $a = 50$ nm and circular (A), square (B), and triangular (C) NPs. AFM images of ThMo nanopatterns with $d = 180$, $a = 50$ nm and circular (D), square (E), and triangular (F) NPs.

code) method. In both calculations, we considered four order ThMo lattices with semiinfinite both the glass substrate (BK7) and the air cover, whereas the thicknesses for the Au pillar and ITO layer used were, respectively, 50 nm and 15 nm. An incident laser wavelength of 785 nm, polarized in the plane of the NPs, was used to stimulate the pattern. Refractive indices used for the materials were $n_{air} = 1$, $n_{glass} = 1.51$, $n_{ITO} = 1.78$, while Au was modeled using the Drude parameters [61]. During the calculations, we set a time step (in units of ct) of 10^{-3} µm and a uniform spatial grid with a step size of 5 nm in each direction. Perfectly matched layer (PML) boundary conditions on all directions were used. The electric component (Ex) intensity, parallel to the substrate surface, was calculated 20 nm above the plane of the NPs to avoid stair-stepped approximation error [62]. The distributions relative to ThMo with $a = 80$ nm and different NPs shape are shown in Figure 2. Calculated fields are quite regular in each nanopattern, and they are generated by both plasmonic and photonic coupling [63, 64]. Field properties are similar for square and circular NPs, with a distribution more uniform in the case of square NPs. In the case of triangular NPs, the near-field achieved seems to be much more localized between two close elements and it decreases rapidly moving away from them. In this last case, the simulations show the highest value for the hotspot area.

Spectral response in transmission was obtained by means of fast Fourier transform (FFT) of the response time. Spectra relative to ThMo with square NPs, $a = 100$ nm, and calculated in three different medium (air, water, and anisole) are reported.

2.3 Spectroscopic characterization

Optical properties of the fabricated plasmonic nanostructures have been evaluated via UV-vis adsorption spectroscopy based on intensity interrogation and SERS. UV-vis extinction measurements allow to investigate the LSPR of the nanostructures, and they were realized using the setup shown in Figure 3A. White light of an unpolarized halogen source is coupled in a microscope and focused on the nanopattern under investigation by an objective (M, 40×; NA, 0.65). The transmission signal is then coupled in a fiber with a core of 50 µm and detected using an Ocean Optics USB4000 spectrometer. We experimentally determined both the bulk refractive index sensitivity (m) and the FOM, defined as the ratio between m and the full wave at half maximum (FWHM) of the nanosensors, by

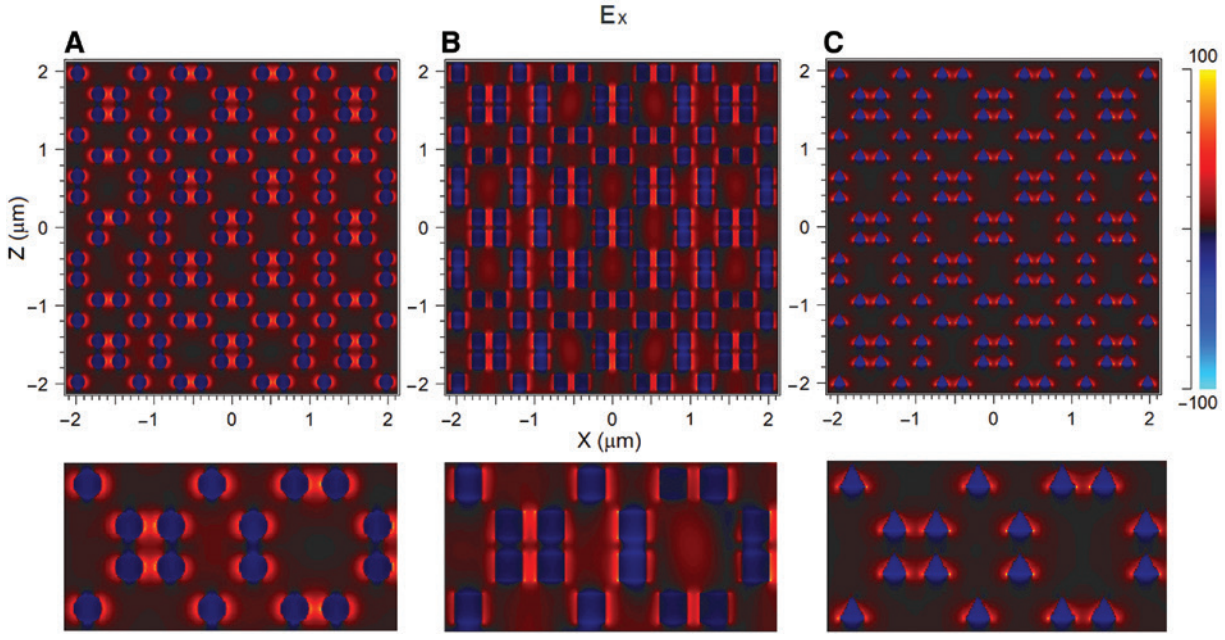

Figure 2: Electric component (Ex) distributions calculated by FDTD method for plasmonic ThMo nanostructures with minimum interparticle distance $a = 80$ nm and different NPs shape: (A) circular, (B) square, (C) triangular.

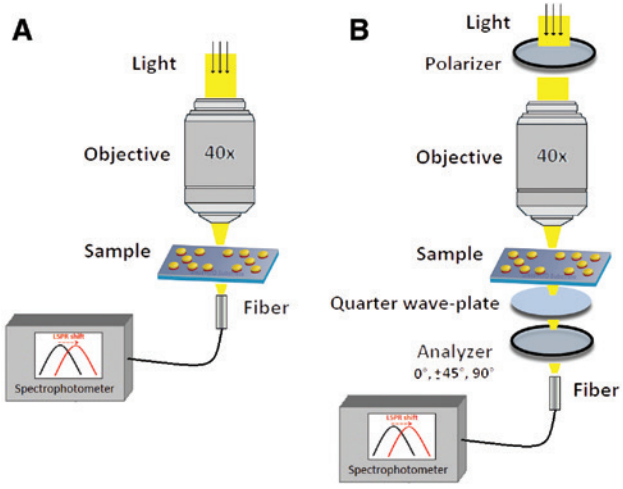

Figure 3: Representation of the experimental set up used for plasmonic measureaments.
(A) Set up used to measure UV-vis extinction spectra. (B) Phase-sensitive setup based on common-path phase quadrature interferometry used for LOD evaluation of Thiram pesticide.

measuring the LSPR peak shift ($\Delta\lambda s$) induced by a change of the medium refractive index: air ($n = 1$), water ($n = 1.332$), glicerin (1.454), and anisole ($n = 1.516$).

SERS measurements were performed using a QE Pro-Raman spectrometer (Ocean Optics) preconfigured for 785 nm (10 mW) Raman excitation, using a 1200 lines/mm grating, and 50-μm slit coupled to an upright laboratory microscope (Olympus BX51). A $50\times$(NA = 0.75) objective was used to focus the laser beam on the nanostructured surfaces and to collect the scattered light in the range of 400–1400 cm^{-1} using a backscattering configuration.

2.4 Modification of nanostructured surface

N,N-dimethylcarbamodithioate (Thiram) is purchased from Merck. A 2.0×10^{-2}–mol l^{-1} Thiram stock solution was prepared by dissolving 0.241 g of Thiram in distilled water and diluting to 50 ml in a volumetric flask. Working solutions were prepared by adequate dilution of the stock solution. Chemisorption of Thiram on the Au nanostructured substrate is simply obtained by depositing on the sample a solution of Thiram for 12 h (overnight). In these experimental conditions, the adsorption of the molecule on the gold surface is guaranteed, due to the presence in the molecule of thioamide (R1-(N-C = S)-R2) groups linked by a disulfide (-S-S-) (see inset in Figure 4C). After 12 h, the sample is washed many times with H_2Odd, IPA and is dried under N_2 flux, before analysis.

3 Results and discussion

In this work, we developed LSPR-based sensors with Au NPs arranged in a ThMo lattice with different geometries fabricated on ITO-coated glass. In Figure 5A–C, we show the extinction spectra measured for ThMo nanopatterns

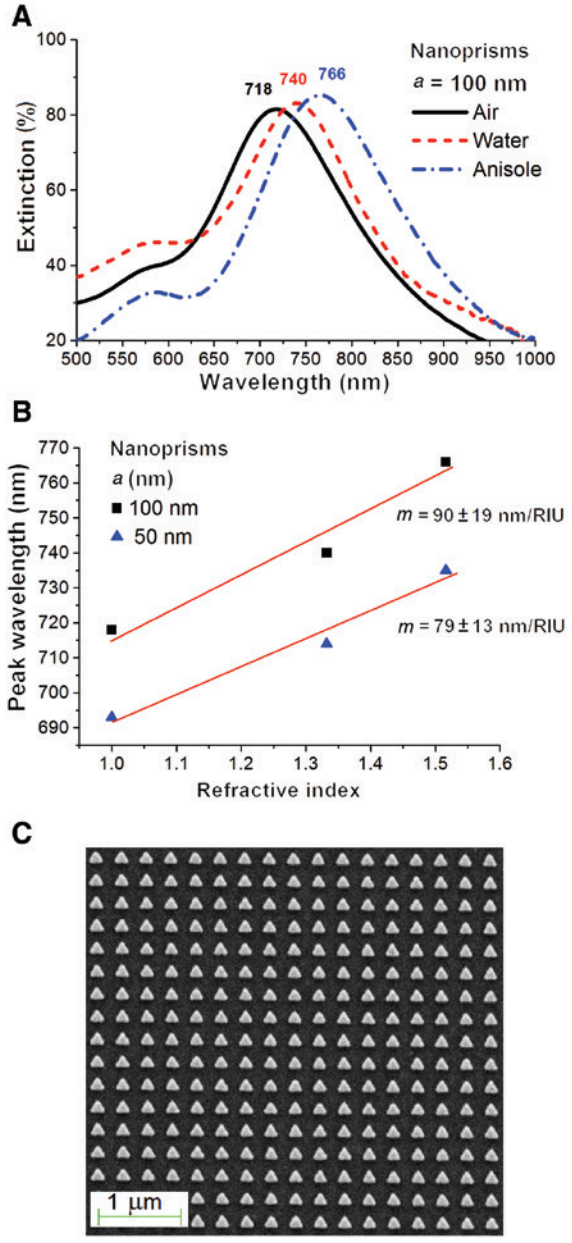

Figure 4: Extinction spectra of a periodic nanopattern based on nanoprisms with $d = 180$ nm and $a = 100$ nm (A).
Trends of the LSPR peak wavelength versus the refractive index of the medium achieved for the nanoprisms array with $a = 50$ nm and $a = 100$ nm (B). SEM image of the nanoprisms pattern with $a = 100$ nm (C).

with $a = 100$ nm. In all cases, the LSPR peaks are located in the NIR region and show a red shift for higher refractive index of the medium as expected. In Figure 5D–F, we report the experimental trends of the LSPR peaks versus the refractive index of the medium achieved for the ThMo investigated with different pillar shape and a parameter. The trend is linear in each case, yielding a higher value of m when a increases. In Figure 5B and E are shown the numerical simulations concerning the extinction spectra (in grey color) of the ThMo with square NPs. Calculated spectra are in good agreement with the experimental ones showing the same red shift and LSPR peaks near those found in the experiment. We ascribe the differences between experimental and simulated spectra to the approximations made in the calculations, in particular, related to the smallest order of the pattern ThMo taken into account (four orders) necessary to reduce the computation time. In Table 1, we report the experimental m values in nm/RIU estimated through the linear fit of the equation $\Delta\lambda s = m\Delta n$ and the FOM achieved for each nanosensor investigated. Our measurements reveal the highest value of m for the ThMo arrangement with square NPs with a maximum $m = 275$ nm/RIU for $a = 100$ nm. At first glance, we can ascribe the higher m of square NPs arrays to their higher reference plasmon wavelength peak (in air) compared to those of circular and triangular ones, but a more in-depth analysis can be made by taking into account the numerical computations realized.

From the comparison between the near fields simulated (Figure 2) and experimental results, it is worth noting that we found higher experimental m values corresponding with field distributions that appear more uniform and less localized. In particular, FDTD simulations show clearly, as in regions far from the NPs where the near-field distribution is due mainly to the photonic coupling and to the multi-scattering process, that the field intensity for the three kinds of ThMo considered is higher in the case of NPs with square shape compared to those of the circular and triangular shapes. This achievement perfectly matches the trend of the experimentally measured sensitivity shown in Table 1. This agreement can be explained by referring to the unique optical interaction properties of aperiodic nanopattern. Due to the increased structural disorder, the aperiodic arrays are strongly coupled in both the plasmonic near-field regime (short-range coupling), which mainly determines the presence of hot-spot area between two near pillars, and the photonic diffractive one (long-range coupling), which essentially affects the field distribution in nanopattern regions far from the particles [63]. In particular, the efficient photonic coupling in aperiodic arrays, associated with their high number of in-plane multi-scattering processes, enables both enhanced field states that are spatially distributed over larger areas and higher photon dwelling times compared to periodic patterns where scattered photons easily escape from the surface. In fact, these characteristics improve the light-analyte interaction, enhancing the sensitivity of the system and making these types of patterns promising to develop advanced sensing devices.

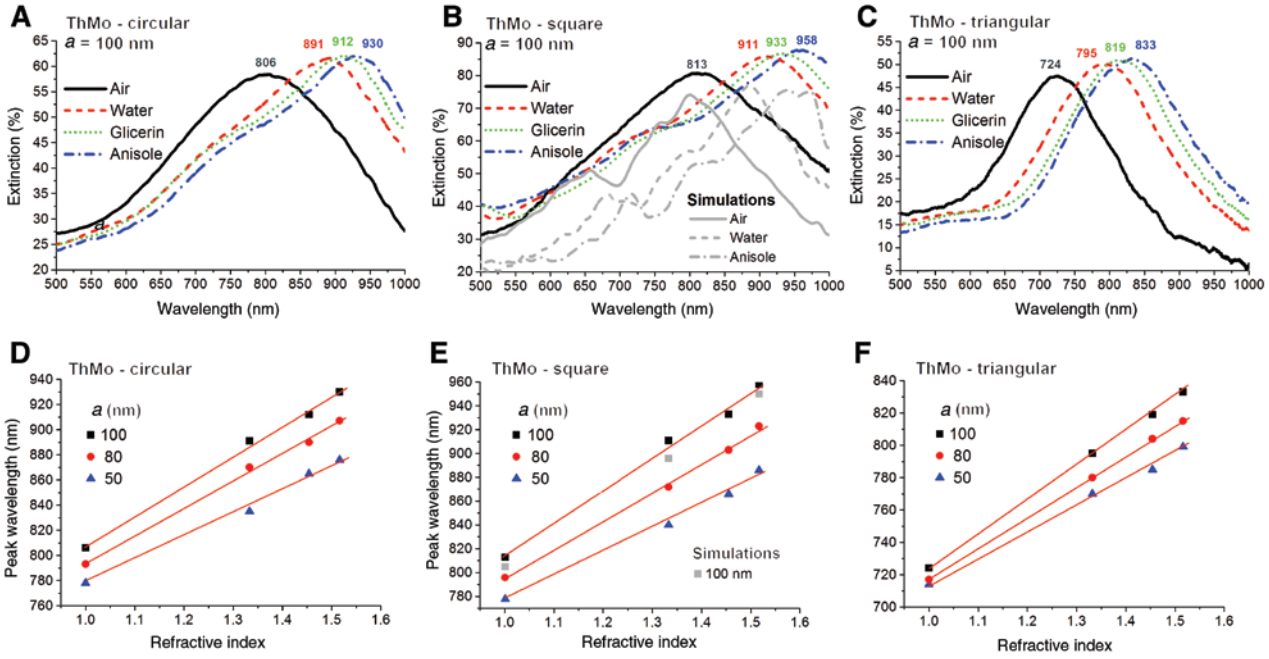

Figure 5: Size- and shape-dependent optical properties of Au NPs in ThMo arrangement.
Extinction spectra of ThMo nanopatterns with $d = 180$ nm, $a = 100$ nm and circular (A), square (B), and triangular (C) NPs. Trends of the LSPR peak wavelength versus the refractive index of the medium achieved for ThMo investigated with different minimum interparticle distance a and circular (D), square (E), and triangular (F) NPs. In (B) and (E), the spectral response obtained by numerical simulations is reported in grey color.

Table 1: FOM and bulk refractive index sensitivity (m) estimated for ThMo nanosensors investigated using the linear fit $\Delta\lambda s = m\Delta n$.

Nanopillars shape	a (nm)	m (nm/RIU)	FOM (RIU^{-1})
Circular	50	190 ± 4	0.74 ± 0.02
	80	218 ± 5	0.83 ± 0.02
	100	238 ± 5	0.89 ± 0.02
Square	50	207 ± 6	0.66 ± 0.02
	80	248 ± 8	0.78 ± 0.03
	100	275 ± 7	0.84 ± 0.02
Triangular	50	161 ± 3	0.98 ± 0.02
	80	190 ± 2	1.14 ± 0.02
	100	212 ± 4	1.24 ± 0.03

Therefore, we can assert that the higher m of square NPs array should arise from the better long-range coupling and higher number of light scattering process enabled from this geometry compared to the ones possible for ThMo arrays made of circular or triangular NPs.

In order to confirm this thesis and highlight the impact that the long-range coupling can have on the sensor performance, we characterized a periodic pattern based on Au nanoprisms with size comparable to those of the ThMo arrays. Figure 4 reports the extinction spectra relative to the pattern with $a = 100$ nm (a), the trends of the LSPR peak wavelength versus the refractive index of three different medium (air, water, and anisole) and the SEM image of the nanoprisms array with $a = 100$ nm (c). The bulk refractive index sensitivity (m) values estimated for the nanoprisms pattern with $a = 50$ nm and $a = 100$ nm, respectively, of 79 nm/RIU and 90 nm/RIU are less than half of those measured for ThMo configurations with comparable size (see Table 1). This gap on the sensitivity found in the comparison of the two kinds of nanostructures investigated (periodic and aperiodic) provides further support to the high impact that the higher number of multi-scattering process in a pattern with greater degree of disorder can have in the realization of sensors with a detection more accurate and sensitive.

Such results show how the nanopatterns considered are well suited as LSPR sensor for detection application of analytes through the use of a low-cost experimental setup. As the results of the characterization in terms of sensitivity m and linearity were promising, we used this approach to investigate an analyte of environmental interest. Nevertheless, the values of FOM found for all nanopatterns analyzed, ranging from 0.66 to 1.24 (Table 1), are not high enough to achieve an optimized very low LOD [65].

In this regard, we further investigated the sensing performance of the ThMo arrays in the detection of the Thiram

pesticide by the use of a common-path phase quadrature interferometry setup, described in the references [52, 53], in a transmission configuration (see Figure 3B). This experimental approach allows more accurate signals with FWHM of few nanometers and hence optimized FOM, enabling lower LOD. In the setup, polarized white light is focused on the nanostructured sensor by an objective (M, 40×; NA, 0.65) and the transmission signal goes through both an achromatic quarter wave plate fixed with the fast axis being placed at 45° with respect to the incident plane and a rotatable analyzer. The signal is then coupled in a fiber with a core of 50 μm and detected using an Ocean Optics USB4000 spectrometer. Four normalized transmission spectra are measured with the analyzer sequentially set at 0°±45° and 90° with respect to the incident plane and considering the transmission measured outside the nanopattern as reference signal. Using the Jones matrix method to describe, the polarized light propagation can be shown as the phase difference φ determined as $\tan\varphi(\lambda)=(I_0(\lambda)-I_{90}(\lambda))/(I_{45}(\lambda)-I_{-45}(\lambda))$, where I_0, $I_{\pm45}$, and I_{90} are, in our case, the normalized transmission spectra taken at different analyzer angles [52]. Unlike the case of symmetrical NPs (square or circular), for triangular NPs, due to their asymmetry, the transmission spectra measured for the *s* and *p* polarizations are shifted [54]. This spectral shift produces a large phase difference φ between the two polarized waves and, consequently, narrow signal lines corresponding to an LSPR peak. For this reason, we used the ThMo array with triangular NPs and a = 100 nm to evaluate the LOD for Thiram. Here, LOD is defined as the minimum detectable refractive index change due to the presence of the pesticide. Analyte aqueous solutions were carefully dropped onto the nanopattern and dried in air under ambient conditions prior to LSPR and SERS measurements. Chemisorption of Thiram on the gold nano-structured surface of our sensor is facilitated by the presence of sulfur in the molecular structure of the compound. The presence of sulfur in the thioamide groups of a disulfide-based molecule surely allows its adsorption on the Au surface. The LOD for Thiram was evaluated through the measurements of the LSPR peaks shift obtained for different molecular concentrations. Figure 6A shows the phase difference φ evaluated for Thiram concentrations ranging between 10^{-5} M and 10^{-9} M analyzed.

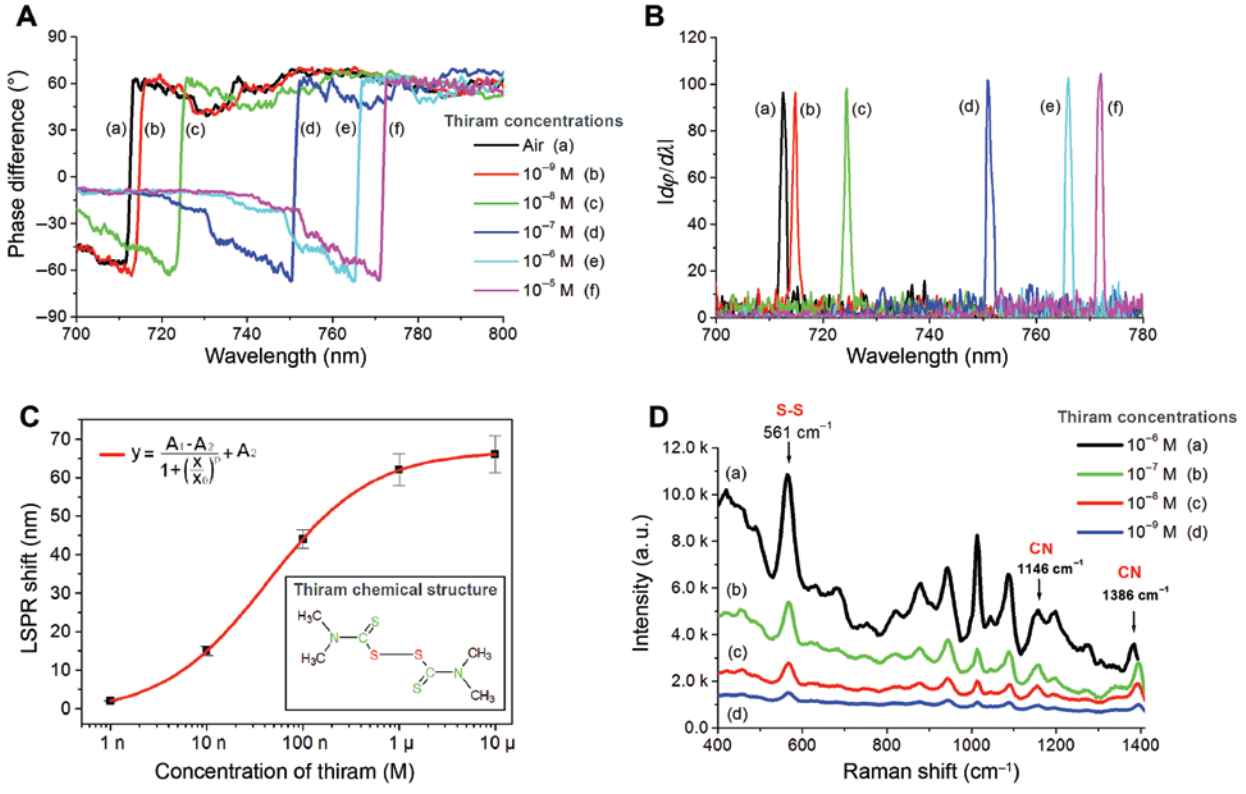

Figure 6: Measurements on ThMo with triangular NPs with d=180 nm and minimum interparticle distance a=100 nm realized for different concentrations of Thiram pesticide: (A) phase difference spectra; (B) absolute differential phase $|d\varphi/d\lambda|$ associated to resonance peaks; (C) plot of resonant wavelength shift versus different concentrations of Thiram, the red line indicates the fit of the logistic sigmoid function and, in the inset, the chemical structure of the Thiram; (D) SERS spectra of different concentrations of Thiram achieved with a laser wavelength of 785 nm.

We characterize the steepness of the phase jumps by calculating the absolute differential phase $|d\varphi/d\lambda|$ in Figure 6B. The signal peaks show a good signal-to-noise ratio, and their FWHMs are found to vary between 1.1 and 1.4 nm, which correspond to the lowest and highest spectral FOM achieved of 151/RIU and 193/RIU, respectively. It is worth noting how the phase-sensitive measurements performed allow signals with line widths about 100 times narrower compared to their intensity-based counterparts. In Figure 6C, the signal wavelength shifts are plotted as a function of the Thiram concentrations. Each data point is the average value of measures relative to four different sensors analyzed with identical concentrations. Data points are well fitted from the logistic sigmoid function (Figure 4C, red line) $y=((A_1-A_2)/(1+(x/x_0)^p)+A_2$ with $A_1=-1.13\pm0.23$, $A_2=-66.90\pm0.14$, $x_0=(4.28\pm0.06)\times10^8$ and $p=0.80\pm0.01$. Considering the intersection of the function with the x axis, we evaluate LOD of 260 ± 70 pM, where the total error has been estimated by the sum in quadrature.

Furthermore, we used Thiram as molecular analyte to evaluate the SERS activity of the same ThMo array and to verify the physical adsorption of the substrate as a function of different concentrations of the Thiram molecules. Figure 6D shows the SERS spectra obtained in which some characteristic peaks of the molecule can be clearly identified: 1386 cm^{-1} attributed to CN stretching mode and symmetric CH_3 deformation mode, 1146 cm^{-1} attributed to CN stretching vibrations mode, and 561 cm^{-1}, which is the S-S stretching mode [66, 67].

4 Conclusions

In summary, we have extensively analyzed the characteristics of the LSPR of engineered aperiodic nanostructures with the arrangement in ThMo NPs as a function of both their shapes and interparticle distances, comparing experimental and numerical results. We experimentally obtained a high m value of 275 nm/RIU with an LSPR sensor using a low-cost setup based on intensity interrogation of easily implementation.

Our results have shown that FOM in based refractive index sensing can be largely increased by measuring the phase difference of the transmitted beam instead of its intensity only. We used our nanosensors for the detection of Thiram pesticide, and to the best of our knowledge, this is the first time that this is done using the LSPR approach and devices fabricated with a top-down technique. An FOM of 193/RIU with a ThMo based on triangular NPs was found. The improved FOM results in an LOD of the pesticide as low as 260 pM (62 pg/ml), which is highly promising for label-free and real-time analysis of solutions at ultralow analyte concentrations.

These achievements demonstrate that the ThMo pattern may be employed for the development of advanced LSPR sensors. The possibility to use this pattern in a dual-mode sensor (SERS + LSPR approaches) makes it more versatile from an application point of view and reduces the cost-effectiveness ratio of these nanosensors.

In conclusion, this work presents significant developments in the use of LSPR sensors based on aperiodic nanopatterns for the detection of pesticides in samples of water. Our results open the possibilities to engineer low-cost portable sensors for the detection of biological and environmental analytes, sensitively, rapidly, and in low volume samples.

Acknowledgments: This work was supported by the European Regional Development Fund-FESR of POR Campania 2007–2013 – Call Innovation Window (Project title: Kit for Brucella Abortus e B. Melitensis nano-Biosensing Rapid detection – AMBRA). We thank Dr. E. Bobeico from ENEA Research Centre of Portici for her support in the fabrication process of the nanostructures and Dr. D. Chen from the Institute of Photonics of Ningbo University for AFM analysis.

References

[1] Sonntag MD, Klingsporn JM, Zrimsek AB, Sharma B, Ruvuna LK, Van Duyne RP. Molecular plasmonics for nanoscale spectroscopy. Chem Soc Rev 2014;43:1230–47.
[2] Shahbazyan TV, Stockman MI, eds. Plasmonics: theory and applications. challenges and advances in computational chemistry and physics 15. Netherlands, Springer 2013;ISBN 978-94-007-7804-7.
[3] Harper MM, McKeating KS, Faulds K. Recent developments and future directions in SERS for bioanalysis. Phys Chem Chem Phys 2013;15:5312–28.
[4] Vendrell M, Maiti KK, Dhaliwal K, Chang YT. Surface-enhanced Raman scattering in cancer detection and imaging. Trends Biotechnol 2013;31:249–57.
[5] Xie W, Schlucker S. Medical applications of surface-enhanced Raman scattering. Phys Chem Chem Phys 2013;15:5329–44.
[6] Aroca RF. Plasmon enhanced spectroscopy. Phys Chem Chem Phys 2013;15:5355–63.
[7] Anker JN, Hall WP, Lyandres O, Shah NC, Zhao J, Van Duyne P. Biosensing with plasmonic nanosensors. Nat Mater 2008;7:442–53.
[8] Li DW, Zhai WL, Li YT, Long YT. Recent progress in surface enhanced Raman spectroscopy for the detection of environmental pollutants. Microchim Acta 2014;181:23–43.

[9] Petti L, Capasso R, Rippa M, et al. A plasmonic nanostructure fabricated by electron beam lithography as a sensitive and highly homogeneous SERS substrate for bio-sensing applications. Vib Spectro 2016;82:22–30.
[10] Zeng S, Baillargeat D, Hod HP, Yong KT. Nanomaterials enhanced surface plasmon resonance for biological and chemical sensing applications. Chem Soc Rev 2014;43:3426–52.
[11] Vo-Dinh T, Fales AM, Griffin GD, et al. Plasmonicnanoprobes: from chemical sensing to medical diagnostics and therapy. Nanoscale 2013;5:10127–40.
[12] Zheng J, He L. Surface-enhanced Raman spectroscopy for the chemical analysis of food. CRFSFS 2014;13:317–28.
[13] Fang Z, Zhu X. Plasmonics in nanostructures. Adv Mater 2013;25:3840–56.
[14] Hughes J, Izake EL, Lott WB, Ayoko GA, Sillence M. Ultra sensitive label free surface enhanced Ramanspectroscopy method for the detection of biomolecules. Talanta 2014;130:20–5.
[15] Luo SC, Sivashanmugan K, Liao JD, Yao CK, Peng HC. Nanofabricated SERS-active substrates for single-molecule to virus detection in vitro: a review. Biosens Bioelectron 2014;61:232–40.
[16] Unser S, Bruzas I, He J, Sagle L. Localized surface plasmon resonance biosensing: current challenges and approaches. Sensors 2015;15:15684–716.
[17] Bingham JM, Hall WP, Van Duyne RP. Exploring the unique characteristics of LSPR biosensing, nanoplasmonic sensors. Springer New York, 2012, Ch. 2.
[18] Stuart DA, Haes AJ, Yonzon CR, Hicks EM, Van Duyne RP. Biological applications of localised surface plasmonic phenomenae. IEE Proc Nanobiotechnol 2005;152:13.
[19] Hammond JL, Bhalla N, Rafiee SD, Estrela P. Localized surface plasmon resonance as a biosensing platform for developing countries. Biosensors 2014;4:172–88.
[20] Guo X. Surface plasmon resonance based biosensor technique: a review. J Biophotonics 2012;5:483–501.
[21] Yuan J, Duan R, Yang H, Luo X, Xi M. Detection of serum human epididymis secretory protein 4 in patients with ovarian cancer using a label-free biosensor based on localized surface plasmon resonance. Int J Nanomed 2012;7:2921–8.
[22] Barbillon G, Bijeon JL, Plain J, Royer P. Sensitive detection of biological species through localized surface-plasmon resonance on gold nanodisks. Thin Solid Films 2009;517:2997–3000.
[23] Park JH, Byun JY, Muna H, et al. A regeneratable, label-free, localized surface plasmon resonance (LSPR) aptasensor for the detection of ochratoxin A. Biosens Bioelectron 2014;59:321–7.
[24] Sanders M, Lin Y, Wei J, Bono T, Lindquist RG. An enhanced LSPR fiber-optic nanoprobe for ultrasensitive detection of protein biomarkers. Biosens Bioelectron 2014;61:95–101.
[25] Rippa M, Castagna R, Pannico M, et al. High-performance nanocavities-based meta-crystals for enhanced plasmonic sensing. Opt Data Process Storage 2016;2:7.
[26] Chiam SY, Singh R, Zhang W, Bettiol AA. Controlling metamaterial resonances via dielectric and aspect ratio effects. Appl Phys Lett 2012;97:191906.
[27] Hong Y, Huh YM, Yoon DS, Yang J. Nanobiosensors based on localized surface plasmon resonance for biomarker detection. J Nanomaterials 2012;13:Article ID 759830.
[28] Liu XW, Lin J, Jiang TF, et al. Surface plasmon properties of hollow Auag alloyed triangular nanoboxes and its applications in Sers imaging and potential drug delivery. PIER 2012;128:35–53.
[29] Coronado EA, Encina ER, Stefani FD. Optical properties of metallic nanoparticles: manipulating light, heat and forces at the nanoscale. Nanoscale 2011;3:4042–59.
[30] Wei H, Xu H. Hot spots in different metal nanostructures for plasmon-enhanced Raman spectroscopy. Nanoscale 2013;5:10794–805.
[31] Lin J, Zhang Y, Qian J, He S. A nano-plasmonic chip for simultaneous sensing with dual-resonance surface-enhanced Raman scattering and localized surface plasmon resonance. Laser Photonics Rev 2014;8:610–6.
[32] Walsh GF, Dal Negro L. Engineering plasmon-enhanced Au light emission with planar arrays of nanoparticles. Nano Lett 2013;13:786–92.
[33] Schuller JA, Barnard ES, Cai W, Jun YC, White JS, Brongersma ML. Plasmonics for extreme light concentration and manipulation. Nat Mater 2010;9:193–204.
[34] Forestiere C, Miano G, Boriskina SV, Dal Negro L. The role of nanoparticle shapes and deterministic aperiodicity for the design of nanoplasmonic arrays. Opt Express 2009;17:9648–61.
[35] Chung T, Lee SY, Song EY, Chun H, Lee B. Plasmonic nanostructures for nano-scale bio-sensing. Sensors 2011;11:10907–29.
[36] Haes AJ, Zou S, Schatz GC, Van Duyne RP. A nanoscale optical biosensor: the short range distance dependence of the localized surface plasmon resonance of silver and gold nanoparticles. J Phys Chem B 2004;108:6961–8.
[37] Haes AJ, Zou S, Schatz GC, Van Duyne RP. A nanoscale optical biosensor: the long range distance dependence of the localized surface plasmon resonance of noble metal nanoparticles. J Phys Chem B 2004;108:109–16.
[38] Petti L, Rippa M, Zhou J, Manna L, Zannella M, Mormile P. Novel hybrid organic/inorganic 2D quasiperiodic PC: from diffraction pattern to vertical light extraction. Nanoscale Res Lett 2011;6:1–6.
[39] Vardeny ZV, Nahata A, Agrawal A. Optics of photonic quasicrystals. Nat Photonics 2013;7:177–87.
[40] Petti L, Rippa M, Capasso R, et al. Plasmonic octagonal quasi crystals for surface-enhanced Raman sensing. Adv Dev Mater 2015;1:47–51.
[41] Arie A, Voloch N. Periodic, quasi-periodic, and random quadratic nonlinear photonic crystals. Laser Photon Rev 2010;4:355–73.
[42] Macià E. Exploiting aperiodic designs in nanophotonic devices. Rep Prog Phys 2012;75:036502.
[43] Chen D, Zhou J, Rippa M, Petti L. Structure-dependent localized surface plasmon resonance characteristics and surface enhanced Raman scattering performances of quasi-periodic nanoarrays: measurements and analysis. J Appl Phys 2015;118:163101.
[44] Dal Negro L, Boriskina SV. Deterministic aperiodic nanostructures for photonics and plasmonics applications. Laser Photonics Rev 2011;6:178–218.
[45] Lee SYK, Amsden JJ, Boriskina SV, et al. Spatial and spectral detection of protein monolayers with deterministic aperiodic arrays of metal nanoparticles. Proc Natl Acad Sci USA 2010;107:12086–90.
[46] Dal Negro L, Stolfi M, Yi Y, et al. Photon band gap properties and omnidirectional reflectance in Si/SiO_2Thue–Morse quasicrystals. Appl Phys Lett 2004;84:5186.

[47] Matarazzo V, De Nicola S, Zito G, et al. Spectral characterization of two-dimensional Thue–Morse quasicrystals realized with high resolution lithography. J Opt 2011;13:015602.
[48] Rippa M, Capasso R, Mormile P, et al. Bragg extraction of light in 2D photonic Thue–Morse quasicrystals patterned in active CdSe/CdS nanorod–polymer nanocomposites. Nanoscale 2013;5:331–6.
[49] Moretti L, Mocella V. The square Thue–Morse tiling for photonic application. Philos Mag 2008;88:2275–84.
[50] Zhang HF, Liu SB, Kong XK. Enlarged the omnidirectional band gap in one-dimensional plasma photonic crystals with ternary Thue-Morse aperiodic structure. Physica B 2013;410:244–50.
[51] Sharma VK, Aulakh JS, Malik AK. Thiram: degradation, applications and analytical methods. J Environ Monit 2003;5:717–23.
[52] Cao ZL, Wong SL, Wu SY, Ho HP, Ong HC. High performing phase-based surface plasmon resonance sensing from metallic nanohole arrays. Appl Phys Lett 2014;104:171116.
[53] Wong SL, Ong HC. Phase difference mapping of two-dimensional metallic nanohole arrays. Appl Phys Lett 2012;100:233102.
[54] Chen WY, Lin CH, Chen WT. Plasmonic phase transition and phase retardation: essential optical characteristics of localized surface plasmon resonance. Nanoscale 2013;5:9950–6.
[55] Guo P, Sikdar D, Huang X, et al. Plasmonic core-shell nanoparticles for SERS detection of the pesticide thiram: size- and shape-dependent Raman enhancement. Nanoscale 2015;7:2862–8.
[56] Rastegarzadeh S, Abdali S. Colorimetric determination of thiram based on formation of gold nanoparticles using ascorbic acid. Talanta 2013;104:22–6.
[57] Yuan C, Liu R, Wang S, et al. Single clusters of self-assembled silver nanoparticles for surface-enhanced Raman scattering sensing of a dithiocarbamate fungicide. J Mater Chem 2011;21:16264–70.
[58] Saute B, Premasiri R, Ziegler L, Narayanan R. Gold nanorods as surface enhanced Raman spectroscopy substrates for sensitive and selective detection of ultra-low levels of dithiocarbamate pesticides. Analyst 2012;137:5082–7.
[59] Saute B, Narayanan R. Solution-based direct readout surface enhanced Raman spectroscopic (SERS) detection of ultra-low levels of thiram with dogbone shaped gold nanoparticles. Analyst 2011;136:527–32.
[60] Zheng X, Chen Y, Chen Y, et al. High performance Au/Ag core/shell bipyramids for determination of thiram based on surface-enhanced Raman scattering. J Raman Spectros 2012;43:1374–80.
[61] Maier SA, Brongersma ML, Kik PG, Atwater HA. Observation of near-field coupling in metal nanoparticle chains using far-field polarization spectroscopy. Phys Rev B 2002;65:193408.
[62] Cangellaris AC, Wright DB. Analysis of the numerical error caused by the stair-stepped approximation of a conducting boundary in FDTD simulations of electromagnetic phenomena. IEEE Trans Antennas Propag 1991;39:1518–25.
[63] Gopinath A, Boriskina SV, Feng NN, Reinhard BM, Dal Negro L. Photonic-plasmonic scatteringresonances in deterministic aperiodic structures. NanoLett 2008;8:2423–31.
[64] Dal Negro L, Feng NN, Gopinath A. Electromagnetic coupling and plasmon localization in deterministic aperiodic arrays. J Opt A Pure Appl Opt 2008;10:064013.
[65] Otte MA, Sepulveda B. Figures of merit for refractometric LSPR biosensing. Nanoplasmonic Sensors, Part of the Series Integrated Analytical Systems, chapter 2012;13:317–31.
[66] Sánchez-Cortés S, Domingo C, García-Ramos JV, Aznárez JA. Surface-enhanced vibrational study (SEIR and SERS) of dithiocarbamate pesticides on gold films. Langmuir 2001;17:1157–62.
[67] Kang S, Hwang SY, Lee CJ, Lee MS. SERS of dithiocarbamate pesticides adsorbed on silver surface. ThiramBull Korean Chem Soc 2002;23:1604–10.